

Impact of quadrupole and hexadecapole deformations and associated orientations on a variety of asymmetric nuclear reactions*

Diksha[†] Harshit Sharma[‡] Manoj K. Sharma[§]

Department of Physics and Materials Science, Thapar Institute of Engineering & Technology, Patiala- 147004, Punjab, India

Abstract: The present manuscript investigates the fusion-ER cross-sections of different projectile-target combinations, namely, $^{16}\text{O}+^{148,150}\text{Nd}$, ^{165}Ho , ^{194}Pt , $^{18}\text{O}+^{148}\text{Nd}$, ^{194}Pt , ^{192}Os , $^{19}\text{F}+^{188}\text{Os}$, and $^{30}\text{Si}+^{170}\text{Er}$, consisting of quadrupole (β_2) and hexadecapole (β_4) deformed target nuclei. The study analyzes the influence of higher-order deformations and corresponding orientation criteria adopted for the exploration of the dynamics of the considered nuclei. The influence of these parameters has been studied in terms of capture cross-section (σ_{cap}), compound nucleus (CN) formation probability (P_{CN}), survival probability (W_{sur}), and the fusion-ER cross-sections across center of mass energies ($E_{\text{c.m.}}$). The study recognizes the importance of the fission barrier in determining the survival probability (W_{sur}) of the compound nucleus and subsequently the ER cross-sections. A discrepancy among the calculated and experimental ER cross-sections is observed, particularly in reactions with lower fission barriers. In reactions with a lower fission barrier of formed CN, the level density parameter ratio (a_f/a_n) of the fission and neutron-evaporation channels assists in the study of experimental data.

Keywords: nuclear reaction, fusion, evaporation residue

DOI: 10.1088/1674-1137/ada7d0 **CSTR:** 32044.14.ChinesePhysicsC.49054108

I. INTRODUCTION

Significant experimental and theoretical effort has been made in the last few decades to understand the synthesis and decay of the heavy and superheavy nuclei via heavy-ion fusion reactions [1–8]. These studies focus on the influence of various parameters and properties of interacting nuclei on the dynamics of heavy-ion-induced reactions. Numerous methods have been reported in the literature to study the synthesis and decay dynamics of such reactions. For instance, various theoretical models like the dinuclear system (DNS) model [9, 10], diffusion model [11], macro-microscopic model [12], dynamical Langevin model [13, 14], and fluctuation-dissipation model [15] are used as the fusion-ER decay model to study decay by evaporation residue (ER) through fusion reactions. The fusion-ER model considers various processes that lead to the formation of compound nuclei (CN) and their decay via the emission of a cascade of light particles.

Heavy-ion-induced reactions can be studied via three stages [5, 16–18]. In the first stage, the projectile and target (P-T) come in contact after their potential barrier is overcome and the process is quantized via the capture

cross-section (σ_{cap}). In the second stage, these interacting nuclei fuse to form a compound nucleus (CN). The extent of the formation of CN against the non-compound nucleus (nCN) processes can be determined by the CN formation probability (P_{CN}). The formed CN is then studied via the fusion cross-section (σ_{fus}). When the incident energy of the projectile exceeds the energy required for the production of an intermediate nucleus, the resulting nucleus is called a CN (excited nuclear state). This excited CN becomes stable by decaying to the ground state via the fission channel or emission of light particles like protons, neutrons, α -particles, and gamma radiation. The extent of survival of an excited CN against the fission process and decay via the evaporation of light particles is measured in terms of survival probability (W_{sur}). This process provides a stable residual nucleus in the ground state. Collectively, σ_{cap} , P_{CN} , and W_{sur} produce the fusion-ER cross-section (σ_{ER}).

Ref. [19] demonstrated that the fusion reaction dynamics depend on the properties of the colliding nuclei. Several theoreticians have shown that along with properties like mass and charge number, the deformation and orientation degrees of freedom, angular momentum, and

Received 9 October 2024; Accepted 9 January 2025; Published online 10 January 2025

* Manoj K. Sharma is thankful to DST-SERB (CRG/2021/001144)

[†] E-mail: dpathania1630@gmail.com

[‡] E-mail: hsharma.nph@gmail.com

[§] E-mail: msharma@thapar.edu

©2025 Chinese Physical Society and the Institute of High Energy Physics of the Chinese Academy of Sciences and the Institute of Modern Physics of the Chinese Academy of Sciences and IOP Publishing Ltd. All rights, including for text and data mining, AI training, and similar technologies, are reserved.

excitation energy of the colliding nuclei significantly influence dynamics of the fusion reaction [20–25]. Additionally, the incorporation of higher order deformations such as octupole β_3 and hexadecapole β_4 deformation induces significant changes in the characteristics of the fusion reaction and better explains experimental results in their compact and elongated configurations [26, 27]. For example, in the reactions of $^{16}\text{O}+^{174,176}\text{Yb}$ [28, 29] and $^{14,15}\text{C}+^{232}\text{Th}$ [30], the authors have found evidence of modification in the fusion barrier after the incorporation of hexadecapole deformations β_4 that significantly enhances capture cross-sections. Moreover, studies in the literature have analyzed fusion cross-sections by incorporating higher-order deformations via microscopic models [31–34]. The optimum orientations of deformed interacting nuclei are determined with respect to the barrier height (V_B) and barrier separation or interaction radius (R_B). For instance, the configuration with the smallest interaction radius and maximum barrier height is called a compact configuration and also known as the belly-to-belly configuration, while the configuration with the largest interaction radius and the minimum barrier height is said to be the elongated configuration or the pole-to-pole configuration [20].

Numerous efforts with different theoretical approaches are used to investigate ER cross-sections via fusion reactions. However, it would be interesting to study the relevance of β_2, β_4 deformations along with their respective 'compact or elongated' orientation degrees of freedom for evaluating fusion-ER cross-sections. Thus, in the present work, the fusion-ER cross-sections are investigated for reactions of the hexadecapole (β_4) deformed targets $^{148,150}\text{Nd}$, ^{165}Ho , ^{194}Pt , $^{188,192}\text{Os}$, and ^{170}Er with spherical $^{16,18}\text{O}$ and β_4 -deformed ^{19}F , ^{30}Si projectile beams for center of mass energies ($E_{\text{c.m.}}$) spread across a Coulomb barrier. The fusion-ER cross-sections are calculated for the considered reactions by incorporating the β_2, β_4 deformations at their respective compact and elongated configurations. Additionally, cross-sections integrated over all orientations are also calculated to provide more extensive insight. The obtained fusion-ER cross-sections are then compared with available experimental data [18, 35–39].

In the present work, fusion-ER cross-sections for a set of reactions are calculated using the semi-classical approach. In this approach, the fusion-ER cross-sections are determined by using the capture cross-sections (σ_{cap}), compound nucleus formation probability (P_{CN}), and survival probability (W_{sur}). The capture cross-sections (σ_{cap}) are calculated using the extended ℓ -summed Wong model incorporating deformations β_2, β_4 at compact, elongated configurations with the proximity potential [40]. The compound nucleus formation probability (P_{CN}) dependent on the Coulomb parameter and center of mass energies ($E_{\text{c.m.}}$) is determined using the Siwek-Wilczyńska

formula [41]. To calculate the survival probability (W_{sur}) of the CN against fission, a statistical model is used [42]. In addition to the deformations and orientations, the influence of the level density parameter ratio between the fission channel to neutron evaporation channel (a_f/a_n) is studied to determine the fusion-ER cross-sections.

The manuscript is organized as follows: Section II provides the formalism for the calculation of the fusion-ER cross-section via the capture cross-section, compound nucleus formation probability, and survival probability. Section III discusses the results and Section IV summarizes them.

II. METHODOLOGY

The fusion-ER cross-sections calculated using the semi-classical approach after the emission of x -number of neutrons from the excited compound nucleus is defined by the product of capture cross-section (σ_{cap}), compound nucleus (CN) formation probability (P_{CN}), and survival probability of the compound nucleus (W_{sur}) is given by

$$\sigma_{\text{er}}^{\text{ER}} = \sigma_{\text{cap}} \times P_{\text{CN}} \times W_{\text{sur}}, \quad (1)$$

and the fusion cross-section of the formed CN is determined as

$$\sigma_{\text{fus}} = \sigma_{\text{cap}} \times P_{\text{CN}}. \quad (2)$$

A. Capture cross-sections

The capture cross-section of deformed and oriented nuclei colliding with the center of mass energies ($E_{\text{c.m.}}$) is determined by using the extended ℓ -summed Wong Model [43]. This includes the sum of the cross-section corresponding to each ℓ -partial wave and is expressed as

$$\sigma_{\text{cap}}(E_{\text{c.m.}}, \theta_i) = \sum_{\ell=0}^{\ell_{\text{max}}} \sigma_{\ell} = \frac{\pi}{k^2} \sum_{\ell=0}^{\ell_{\text{max}}} (2\ell + 1) P_{\ell}, \quad (3)$$

where $k = \sqrt{\frac{2\mu E_{\text{c.m.}}}{\hbar^2}}$ and μ is the reduced mass. Here, the sharp cut-off approximation [44, 45] is used to calculate the maximum angular momentum denoted by ℓ_{max} .

Wong approximated barrier penetration for different ℓ -waves using the inverted harmonic oscillator potential with barrier height $V_B^{\ell}(E_{\text{c.m.}})$, interaction radius $R_B^{\ell}(E_{\text{c.m.}})$, and curvature $\hbar\omega_B^{\ell}(E_{\text{c.m.}})$. Thus, the penetration probability P_{ℓ} across the barrier for each ' ℓ ' is given by the Hill-Wheeler approximation [46]:

$$P_{\ell}^{\text{HW}}(E_{\text{c.m.}}) = \left[1 + \exp\left(\frac{2\pi[V_B^{\ell}(E_{\text{c.m.}}) - E_{\text{c.m.}}]}{\hbar\omega_B^{\ell}(E_{\text{c.m.}})}\right) \right]^{-1}. \quad (4)$$

$V_B^\ell(E_{c.m.})$, $R_B^\ell(E_{c.m.})$, and $\hbar\omega_B^\ell(E_{c.m.})$ are obtained from the total interaction potential between the two interacting nuclei, which is the sum of the repulsive Coulomb (V_C) and centrifugal (V_ℓ) potentials, and attractive nuclear potential (V_N). The total potential $V_T(R_i, A_i, \beta_{\lambda i}, \theta_i)$ is therefore calculated as follows:

$$V_T(R_i, A_i, \beta_{\lambda i}, \theta_i) = V_C(R_i, A_i, \beta_{\lambda i}, \theta_i) + V_\ell(R_i, A_i, \beta_{\lambda i}, \theta_i) + V_N(R_i, A_i, \beta_{\lambda i}, \theta_i). \quad (5)$$

The radius vector $R_i(\alpha_i)$ can be used to express the shape of the deformed nuclear surface, which involves the spherical harmonic wave functions $Y_\lambda^{(0)}(\alpha_i)$ of higher-order deformations $\beta_{\lambda i}$, where $\lambda = 2, 3, 4$ are the orders of quadrupole, octupole, and hexadecapole deformed shapes, respectively [47–50]:

$$R_i(\alpha_i) = R_{0i} \left[1 + \sum_{\lambda=2,3,4} \beta_{\lambda i} Y_\lambda^{(0)}(\alpha_i) \right] = R_{0i} \left[1 + \sum_{\lambda=2,3,4} \beta_{\lambda i} \sqrt{\frac{2\lambda+1}{4\pi}} P_\lambda(\cos \alpha_i) \right]. \quad (6)$$

In this case, the projectile and target nuclei are denoted by $i = 1$ and 2 , respectively.

$R_{0i} = 1.28A_i^{1/3} - 0.76 + 0.8A_i^{-1/3}$, measured in fm [40], represents the radius of the spherical nuclei. The deformation parameter $\beta_{\lambda i}$ was obtained from the Table of Möller *et al* [49]. $P_\lambda(\cos \alpha_i)$ is the Legendre polynomial.

The Coulomb potential (V_C) in Eq. (5) is defined as follows for deformed-deformed colliding nuclei [43]:

$$V_C(R) = \frac{Z_1 Z_2 e^2}{R} + Z_1 Z_2 e^2 \sum_{\lambda=2,3,4}^{i=1,2} \left(\frac{R_i^\lambda(\alpha_i)}{R^{\lambda+1}} \right) \beta_{\lambda i} Y_\lambda^{(0)}(\theta_i) \times \left[\frac{3}{2\lambda+1} + \left(\frac{12}{7(2\lambda+1)} \right) \beta_{\lambda i} Y_\lambda^{(0)}(\theta_i) \right]. \quad (7)$$

While for the spherical-deformed cases, $\beta_{21}, \beta_{41} = 0.0$ are considered. The centrifugal potential (V_ℓ) is represented in the form of rotational kinetic energy and is given as

$$V_\ell(R, A_i, \beta_{\lambda i}, \theta_i) = \frac{\hbar^2 \ell(\ell+1)}{2I}; \quad I = \mu R^2. \quad (8)$$

In Eq. (5), the attractive nuclear potential (V_N) between the two interacting nuclei is determined by the generalized theorem for proximity forces discovered by Blocki *et al.* [40]. According to this theorem, the nuclear potential is the product of $4\pi\bar{R}\gamma b$ and $\Phi(s_0)$. The term $4\pi\bar{R}\gamma b$ depends on the shape and geometry of the colliding nuclei, whereas $\Phi(s_0)$ is a universal function dependent on the shortest distance between the colliding nuclei.

Thus, $V_N(R, A_i, \beta_{\lambda i}, \theta_i)$, called the 'Proximity potential', is given by [40, 44, 51]

$$V_N(R, A_i, \beta_{\lambda i}, \theta_i) = 4\pi\bar{R}\gamma b\Phi(s_0), \quad (9)$$

where, 'b' is the surface thickness and considered to be 0.99 fm.

The mean curvature radius (\bar{R}) is calculated in terms of radius vector of curvatures R_{i1} and R_{i2} for projectile and target nuclei resp., as follows:

$$\frac{1}{\bar{R}^2} = \frac{1}{R_{11}R_{12}} + \frac{1}{R_{21}R_{22}} + \frac{1}{R_{11}R_{22}} + \frac{1}{R_{21}R_{12}}. \quad (10)$$

The principal radii of curvature (R_{i1} and R_{i2}) at the angle of projection w.r.t. the collision axis (α_i) for deformed-deformed or spherical-deformed cases is given [51] by

$$R_{i1}(\alpha_i) = \frac{[R_i^2(\alpha_i) + R_i'^2(\alpha_i)]^{3/2}}{R_i^2(\alpha_i) + 2R_i'^2(\alpha_i) - R_i(\alpha_i)R_i''(\alpha_i)}, \quad (11)$$

$$R_{i2}(\alpha_i) = \frac{R_i(\alpha_i) \sin \alpha_i}{\cos(\pi/2 - \alpha_i - \delta_i)} \quad (i = 1, 2). \quad (12)$$

It is important to note that for spherical projectiles, $R_{11(\alpha_1)} = R_{12(\alpha_1)} = R_1(\alpha_1)$. In Eq. (9), the surface energy constant γ is expressed in terms of asymmetry terms as

$$\gamma = 0.9517 \left[1 - 1.7826 \left(\frac{N-Z}{A} \right)^2 \right] \text{ MeVfm}^{-2}. \quad (13)$$

In Eq. (9), the universal function dependent on the shortest distance parameter s_0 is

$$\Phi(s_0) = \begin{cases} -\frac{1}{2}(s_0 - 2.54)^2 - 0.0852(s_0 - 2.54)^3, & s_0 \leq 1.2511 \text{ fm} \\ -3.437 \exp\left(-\frac{s_0}{0.75}\right), & s_0 > 1.2511 \text{ fm}. \end{cases} \quad (14)$$

Eqs. (5) – (14) outline the total interaction potential and provide valuable information regarding the properties of the interacting nuclei. This includes barrier characteristics such as the barrier height V_B , the barrier position R_B , and the barrier curvature $\hbar\omega_B$. These parameters are influenced by the degrees of freedom associated with deformation and orientation introduced in the radius vector obtained using Eq. (6). Consequently, these variables are utilized in the calculations of capture cross-sections.

In addition, the integrated or average capture cross-

sections are obtained by integrating over the range of orientations θ_i of the deformed nuclei having $\beta_2\beta_4$ deformations, which is represented as

$$\sigma_{\text{int}}(E_{\text{c.m.}}) = \int_{\theta_1=0}^{\pi/2} \int_{\theta_2=0}^{\pi/2} \sigma(E_{\text{c.m.}}, \theta_i) \sin \theta_1 \sin \theta_2 d\theta_1 d\theta_2. \quad (15)$$

B. Compound Nucleus formation probability (P_{CN})

The compound nucleus formation probability P_{CN} provides information about the chances of the formation of a CN, where the fusion cross-section of CN is given by $\sigma_{\text{fus}} = \sigma_{\text{cap}} \times P_{\text{CN}}$. The phenomenological approach for calculating P_{CN} was proposed by Siwek-Wilczyńska [41] and is given by

$$P_{\text{CN}} = 10^{-(z/b)^k}, \quad (16)$$

where k is taken as 3.0 and z is the Coulomb parameter,

$$z = \frac{Z_1 Z_2}{A_1^{1/3} + A_2^{1/3}}, \quad (17)$$

where Z_1, Z_2 represent the atomic number, while A_1 and A_2 represent the the mass numbers of the projectile and target, respectively. Parameter b depends on $E_{\text{c.m.}}$ and mean interaction barrier B [52, 53]:

$$b = 2(E_{\text{c.m.}} - B)/(\text{MeV}) + 135, \quad (18)$$

where B is given by

$$B = (0.85247z + 0.001361z^2 - 0.00000223z^3) \text{ MeV}. \quad (19)$$

C. Survival probability (W_{sur})

The excited CN is cooled by the emission of neutrons instead of fission. The survival probability (W_{sur}) is used to measure CN's resistance to the fission process and can be obtained using a statistical approach [42, 54]:

$$W_{\text{sur}} = P_{xn}(E_{\text{CN}}^*) \times \prod_{i=1}^x \frac{\Gamma_n}{\Gamma_n + \Gamma_f}, \quad (20)$$

where Γ_n and Γ_f are neutron emission and fission decay widths, respectively, and $P_{xn}(E_{\text{CN}}^*)$ the 'Jackson factor'[55] is the probability of the emission of x neutrons from the excited CN at excitation energy E_{CN}^* . B_i is the separation energy of the i^{th} neutron. T is the temperature (in MeV) obtained using the statistical method [56] as

$$E_{\text{CN}}^* = aT^2 - T = E_{\text{c.m.}} + Q,$$

where Q is the Q -value and $a = A/10$ is the level density parameter for a CN with mass number A . In terms of B_i , T , and E_{CN}^* , the P_{xn} is given by

$$P_{xn}(E_{\text{CN}}^*) = I(\Delta_x, 2x - 3) - I(\Delta_{x+1}, 2x - 1), \quad (21)$$

where $I(\Delta_x, 2x - 3)$ is Pearson's incomplete gamma function [57] and $\Delta_x = \frac{(E_{\text{CN}}^* - \sum_{i=1}^x B_i)}{T}$. The classical approach for determining decay width ratios of the i^{th} neutron to fission $\frac{\Gamma_n}{\Gamma_f}$ has been suggested by Vandenbosch and Huizenga [58]:

$$\frac{\Gamma_n}{\Gamma_f} = \frac{4A^{2/3} a_f (E_{\text{CN}}^* - B_i)}{K_0 a_n [2a_f^{1/2} (E_{\text{CN}}^* - B_f)^{1/2} - 1]} \times \exp[2a_n^{1/2} (E_{\text{CN}}^* - B_i)^{1/2} - 2a_f^{1/2} (E_{\text{CN}}^* - B_f)^{1/2}], \quad (22)$$

where B_f is the fission barrier height, which determines the chances of the fission or evaporation of neutrons. The value of the constant $K_0 = \hbar^2 / 2mr_0^2$ is considered to be 10 MeV. The level density parameter of the neutron evaporation channel is $a_n = A/10$ and that of the fission channel is $a_f = 1.1a_n$. The values of a_f are also considered from 1.0 to 1.05 w.r.t a_n . The fission barrier height B_f before the emission of the i^{th} neutron is calculated as the sum of the liquid drop fission barrier B_f^{LD} and shell correction energy B_f^{shell} [54]:

$$B_f(E_{\text{CN}}^*) = B_f^{LD} + B_f^{\text{shell}} \exp(-E_{\text{CN}}^*/E_d), \quad (23)$$

where the B_f^{LD} is determined using the approximate analytic method in [59] and the value of B_f^{shell} is obtained from the Möller and Nix table [49]. $E_d = 5.48A^{1/3} / (1 + 1.3A^{-1/3})$ is the damping factor, which characterizes the decrease in shell effects with the increasing excitation energy of CN.

III. RESULT AND DISCUSSION

This study focused on analyzing the relevance of higher-order deformations (β_2, β_4) on the fusion-ER cross-sections at their respective compact, elongated configurations. To investigate the impact of deformations and orientation degrees of freedom on the fusion-ER cross-section, we considered heavy-ion-induced reactions involving different projectile and target nuclei. For the chosen reactions, the experimental data of ER cross-sections can be obtained from [18, 35–39]. These reactions include the interactions of the hexadecapole (β_4) deformed targets $^{148,150}\text{Nd}$, ^{165}Ho , ^{194}Pt , and ^{192}Os with spherical projectiles $^{16,18}\text{O}$, and β_4 -deformed projectile-target combination ^{19}F and ^{188}Os .

The CN formed using these reactions have the mass range $A = 150 - 212$. The reactions are studied at the center of mass energies ($E_{c.m.}$) lying across the Coulomb barrier shown in Table 1. The static deformations are taken from the Table of P. Möller[49].

Section A discussed the behaviour of the capture cross-section of these reactions as a function of the center of mass energy ($E_{c.m.}$). Section B is dedicated to the fusion cross-sections and Section C covers the analysis of the evaporation residue component.

A. Capture cross-sections

Past research shown that the deformations and orientations (compact and elongated) associated with the interacting nuclei alter the barrier characteristics V_B , R_B , $\hbar\omega$, etc., which further influence the capture cross-sections (σ_{cap}). We have evaluated σ_{cap} by incorporating the deformations (up to β_4) of the interacting nuclei chronologically (*i.e.* β_2 and $\beta_2\beta_4$) at respective compact, elongated orientations (θ_i) and integrating over all the orientations of the considered P-T combinations. The σ_{cap} are calculated within the same plane ($\phi=0$) for the center of mass energies ($E_{c.m.}$) lying across the Coulomb barrier, as depicted in Fig. 1. The ℓ -values used to incorporate angular momentum effects are calculated using the sharp cut-off approximation. Fig. 1 shows different cross-section trends for different combinations of deformations at their respective compact/elongated configurations along with the cross-sections integrated over all the orientations in comparison to the spherical system. For example, the presence of β_2^+ deformation reduces cross-sections in the compact configuration due to a small interaction radius at the highest barrier height. However, in the elongated configurations of β_2^+ , the cross-sections are enhanced relative to the spherical case due to the larger interaction radius at the smallest barrier height, as illustrated in Fig. 1(a-h). Further incorporating β_4^+ deformation in β_2^+ elongates the nuclear shape, which increases the interaction radius. Therefore, the cross-sections are further enhanced for both configurations (*i.e.* compact and elongated) of $\beta_2^+\beta_4^+$

compared to β_2^+ only, which is illustrated in Fig. 1(a-d). For the reactions shown in Fig 1(e-h), the inclusion of β_4^- deformations to the β_2^+ of the target nuclei produces reduced cross-sections in both compact and elongated configurations compared to cross-sections obtained by β_2^+ deformation alone. This suppression is attributed to the compressive effects of β_4^- , reducing the interaction radius relative to β_2^+ . The integrated cross-sections (σ_{int}) obtained for the considered $\beta_2\beta_4$ deformed nuclei represent the average effect of all orientations. These integrated capture cross-sections (σ_{int}) are between the cross-sections obtained by compact and elongated configurations, reflecting the combined effects of nuclear shapes and interaction dynamics across all orientations.

The obtained capture cross-sections σ_{cap} for the various configurations of the deformed nuclei are then compared with experimental ER cross-sections ($\sum \sigma_{yn}^{ER}$), as shown in Fig. 1. This comparison highlights the significance of nuclear deformation and orientation, which subsequently affect the ER cross-sections. The additional parameters for predicting the ER cross-sections such as the CN formation probability and survival probability are discussed in the subsequent sections.

B. Fusion cross-section (σ_{fus})

The previous section emphasizes the importance of incorporating the deformation and orientation degrees of freedom in the capture cross-section, as shown in Fig. 1. At the same time, Fig. 1 provides the idea that the capture cross-sections obtained with the incorporation of β_4 deformation are enhanced. To estimate the fusion-ER cross-section mentioned in Eq. (1), we incorporate the role of the compound nucleus formation probability (P_{CN}). This term determines the extent to which the interaction between projectile and target (P-T) can lead to a fusion state and the creation of CN after the capture process. The fusion cross-section, described in Eq. (2), examines the extent of the CN formation. In the present study, we have analyzed P_{CN} using the Siwek-Wilczyńska formula [41] given in Eq. (16). P_{CN} is influ-

Table 1. Tabulation of the entrance channel properties such as the center of mass energies ($E_{c.m.}$), interaction barrier (V_B), Coulomb factor (z), and fissility parameter (χ) of the formed compound nucleus (CN) at excited energies (E_{CN}^*) for all the considered reactions.

Reaction	CN	$E_{c.m.}$	E_{CN}^*	V_B	z	χ
$^{18}\text{O}+^{148}\text{Nd}$	^{166}Er	55–69	41–56	57.47	60.68	0.581
$^{16}\text{O}+^{150}\text{Nd}$	^{166}Er	55–73	42–59	58.061	61.27	0.581
$^{16}\text{O}+^{148}\text{Nd}$	^{164}Er	58–72	42–56	58.208	61.46	0.584
$^{16}\text{O}+^{165}\text{Ho}$	^{181}Re	66–96	43–73	63.948	66.96	0.644
$^{18}\text{O}+^{192}\text{Os}$	^{210}Po	73–113	52–92	69.896	72.46	0.711
$^{18}\text{O}+^{194}\text{Pt}$	^{212}Rn	75–97	48–70	71.649	74.20	0.732
$^{16}\text{O}+^{194}\text{Pt}$	^{210}Rn	69–96	39–66	72.541	75.101	0.735
$^{19}\text{F}+^{188}\text{Os}$	^{207}At	72–95	42–65	79.097	81.45	0.727

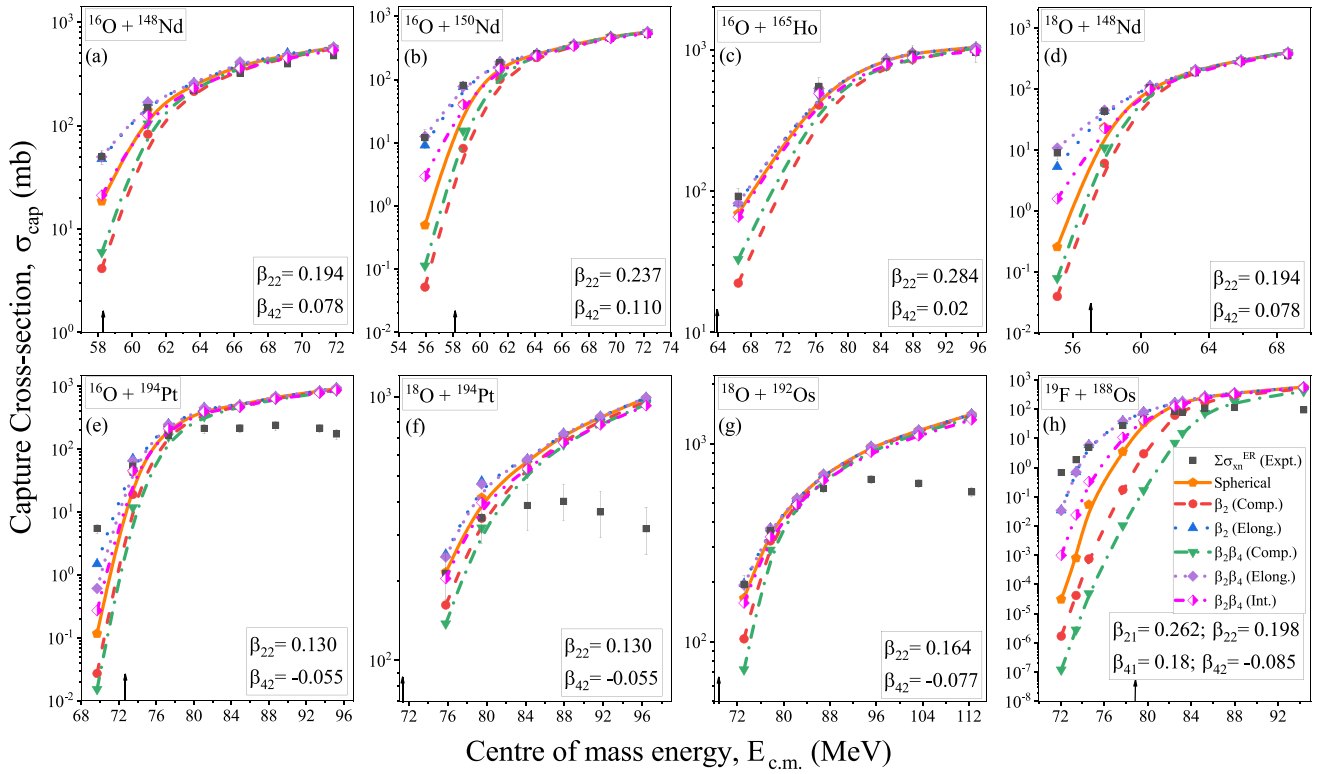


Fig. 1. (color online) Schematic diagram of the capture cross-sections (σ_{cap}) obtained by the extended ℓ -summed Wong model as a function of $E_{\text{c.m.}}$ with spherical, compact, and elongated configurations along with the cross-sections integrated over all orientations for the considered P-T combinations. The black arrow denotes the Coulomb barrier energy corresponding to each P-T combination.

enced by the charge and mass number of the entrance channel. These parameters collectively determine the Coulomb parameter ' z '. ' z ' varies the mean interaction barrier for fusion, denoted as ' B ', which is further used for the calculation of parameter ' b ' at a given $E_{\text{c.m.}}$.

Figure 2 shows the variation of P_{CN} with respect to $E_{\text{c.m.}}$. The calculated P_{CN} for the considered reactions is plotted for the same energy range. Further, P_{CN} increases with increasing $E_{\text{c.m.}}$, implying the increase in the fusion process for the formation of CN. This value approaches 1 with increasing energy. This variation in P_{CN} for all the considered P-T combinations depends on the Coulomb parameter ' z ', which hinders the complete formation of CN. For example, the reactions or the P-T combinations with a smaller Coulomb parameter have higher P_{CN} than those with a higher Coulomb parameter. The $^{16,18}\text{O}$ induced reactions exhibit a higher P_{CN} within the range of 0.7 – 0.9 for the energy range given in Table 1. However, for the ^{19}F induced reaction, the addition of one proton in ^{19}F compared to $^{16,18}\text{O}$ increases the Coulomb parameter, which reduces P_{CN} to values in the range of 0.5 – 0.7. The above discussion makes it evident that the entrance channel plays a crucial role in the formation of CN. This repulsion by the Coulomb parameter is compensated by increasing $E_{\text{c.m.}}$, allowing the P-T combination to facilitate the formation of a CN.

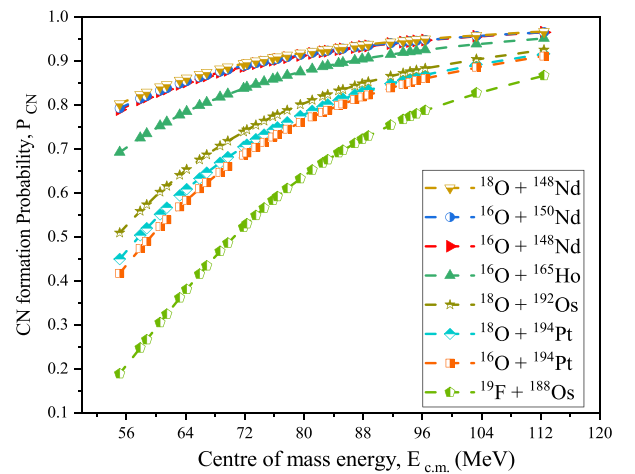


Fig. 2. (color online) Schematic diagram of the variation of the CN formation probability (P_{CN}) with the center of mass energies ($E_{\text{c.m.}}$) for the considered P-T combinations.

The product of P_{CN} with the capture cross-sections (σ_{cap}) gives us the fusion cross-sections (σ_{fus}). The formation of the CN is investigated by analyzing the (σ_{fus}), as mentioned in Eq. (2). The σ_{fus} values for all the considered reactions are compared to the experimental ER cross-section data depicted in Fig. 3. The figure shows

that the fusion component contributes significantly to the capture process, with $P_{CN} \geq 0.7$. To achieve an explicit understanding and better explanation of the ER cross-sections, we must introduce the missing term to examine the relevance of the fission process, i.e., the survival probability of the formed compound nucleus (W_{sur}). This part is addressed in the next section.

C. Evaporation residue cross-section (σ_{xn}^{ER})

The fusion process results in the formation of a CN in an excited nuclear state. The CN stabilizes itself either by emitting light particles or forming fragments through fission. In this study, we examine the possibility of fission by calculating the survival probability W_{sur} of the formed compound nucleus. The survival probability W_{sur} in Eq. (1) represents the chances of a CN transitioning to the ground state by emitting neutrons instead of undergoing fission. The survival probability is calculated using the statistical model described in Eq. (20), which takes into account the probability of neutron emission from the excited state P_{xn} and the ratio of neutron decay width Γ_n to fission decay width Γ_f at a specific excitation energy E_{CN}^* of the CN. The factor P_{xn} depends on the temperature (T), excitation energy (E_{CN}^*) of the CN, and separation energies of the neutrons B_i but is independent of the atomic mass of nuclei. However, the ratio of decay widths depends on the mass number A , fission barrier

height B_f , and neutron separation energy of the CN at a given E_{CN}^* . The survival of the CN against fission is determined by the fission barrier B_f of the CN at that specific E_{CN}^* . The fission barrier B_f is calculated as the sum of the macroscopic part or liquid drop term (B_f^{LD}) and the microscopic shell correction energy (B_f^{Shell}), as described in Eq. (23). The B_f^{Shell} decreases exponentially with increasing E_{CN}^* , resulting in a decrease in B_f with increasing E_{CN}^* , enhancing the fission probability. On the contrary, the values of B_f^{LD} and B_f^{Shell} depend on the mass and atomic number of the formed CN and exhibit different magnitudes of B_f^{LD} and B_f^{Shell} . The B_f^{LD} component arises from the competition between the Coulomb and surface forces, which is determined by the fissility parameter (χ). This parameter χ depends on the mass number 'A' and the charge 'Z' of the CN. The magnitudes of χ obtained for CN in the considered P-T combinations are provided in Table 1. The fissility parameter decreases as the atomic number decreases, causing an increase in B_f^{LD} . As a result, the fission barrier B_f becomes considerably higher compared to B_i for CN in reactions having high B_f^{LD} values and very low shell correction energies, such as $^{16}\text{O}+^{148,150}\text{Nd}$, ^{165}Ho , and $^{18}\text{O}+^{148}\text{Nd}$, leading to a higher likelihood of neutron emissions demonstrated by higher values of W_{sur} . Meanwhile, the fission barrier B_f obtained for compound nuclei having low B_f^{LD} values and significant shell correction in reactions such as $^{16}\text{O}+^{194}\text{Pt}$,

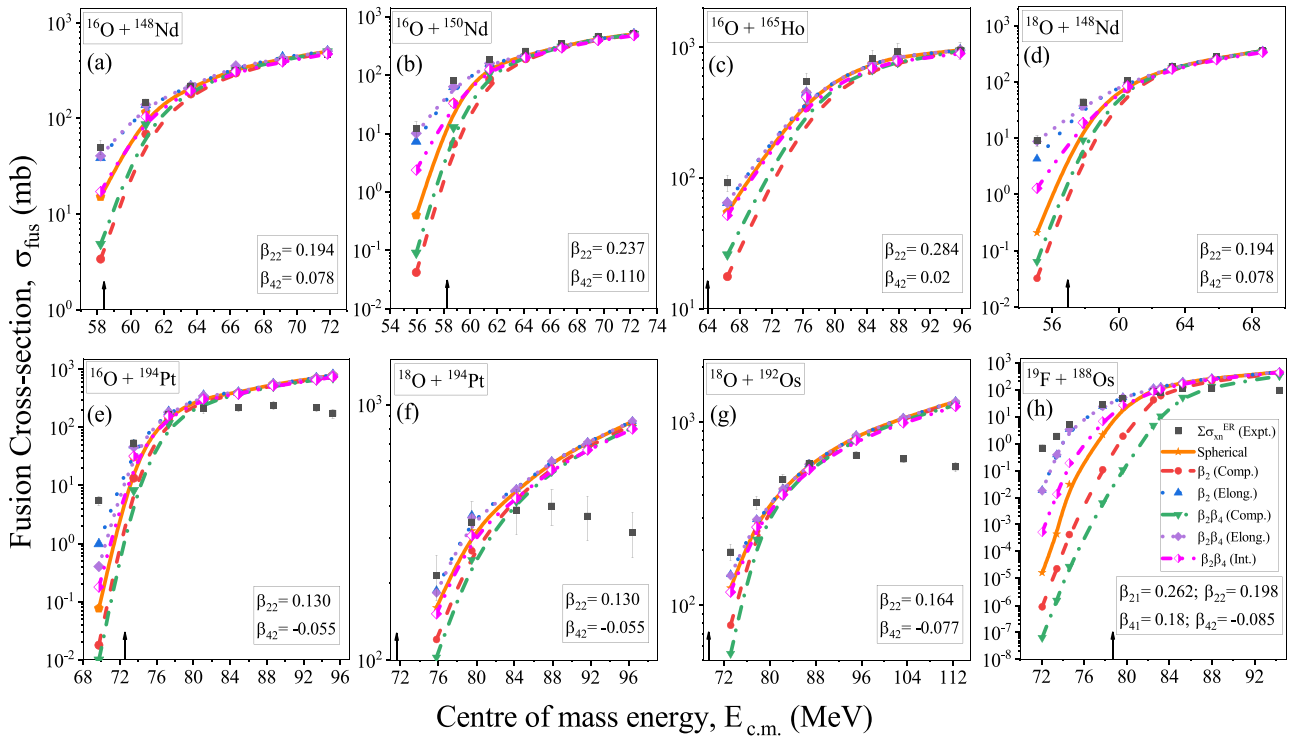


Fig. 3. (color online) Schematic diagram of Fusion cross-sections ($\sigma_{fus} = \sigma_{cap} \times P_{CN}$) as functions of $E_{c.m.}$ with spherical, compact, and elongated configurations along with the cross-sections integrated over all orientations for the considered P-T combination. The black arrow denotes the Coulomb barrier energy corresponding to each P-T combination.

$^{18}\text{O}+^{194}\text{Pt}$, ^{192}Os , and $^{19}\text{F}+^{188}\text{Os}$ is comparable to B_i . Although the higher B_f^{Shell} values of these nuclei having neutron numbers around $N = 126$ do not have a significant impact on B_f [18, 60], as B_f^{Shell} values decrease with increasing E_{CN}^* . Therefore, the decrease in the fission barrier and W_{sur} implies a higher likelihood of the fission process dominating neutron evaporation channels.

As mentioned in Eq. (1), the fusion-ER cross-section is obtained by multiplying the survival probability W_{sur} with the fusion cross-section σ_{fus} . In the previous discussion, we discussed the various factors affecting both the W_{sur} and σ_{fus} and determined their values for the considered P-T combinations. The total fusion-ER cross-sections calculated by summing all the fusion-ER cross-sections for all the neutron channels are compared with experimental data for the considered reactions in Fig. 4. The calculated fusion-ER cross-sections obtained for the ' $\beta_2\beta_4$ ' case for the reactions $^{16}\text{O}+^{148,150}\text{Nd}$, ^{165}Ho , and $^{18}\text{O}+^{148}\text{Nd}$ show good agreement with the experimental data presented in Fig. 4(a-d). However, these calculations do not yield satisfactory results for other reactions $^{16}\text{O}+^{194}\text{Pt}$, $^{18}\text{O}+^{194}\text{Pt}$, ^{192}Os , and $^{19}\text{F}+^{188}\text{Os}$ shown in Fig. 4(e-h) owing to the presence of a small fission barrier, indicating the dominance of fission.

To obtain the desired cross-sections, it has been observed that, apart from the fission barrier, the W_{sur} of the nuclei is also affected by the ratio of level density para-

eters between the fission channel and the neutron evaporation channel (a_f/a_n) [61, 62]. This ratio determines the likelihood of fission in the nuclei. An investigation of W_{sur} for all the contributing neutron channels is conducted in terms of a_f/a_n for the compound nuclei (CN) ^{210}Po , ^{207}At , and ^{210}Rn at a common excitation energy E_{CN}^* . The findings of this analysis are presented in Fig. 5. From the figure, one can observe that as the a_f/a_n ratio increases, the W_{sur} of neutrons decreases and the nucleus is likely to undergo the fission process. The variation of W_{sur} at $E_{\text{CN}}^* = 52$ MeV is associated with the fission barrier height of the CN, as depicted in Fig. 5(a). While $3n$, $4n$, and $5n$ are common neutron decay channels in all of the formed CN, the contribution of neutron channels $6n$ and $7n$ is found in ^{210}Po , and the contribution of $6n$ is found in ^{210}Rn as the excitation energy increases. This result is depicted in Fig. 5(b-d). Hence, to achieve better agreement with experimental results and gain a deeper understanding of cases with lower fission barriers, the calculation of the survival probability should incorporate lower values for this ratio, as the lower value of the ratio indicates the dominance of decay via neutron evaporation.

For instance, the results represented in Fig. 4 are obtained by considering the ratio $a_f/a_n = 1.1$. The sensitivity of the a_f/a_n ratio in the fusion-ER cross-sections is investigated for the reactions $^{16}\text{O}+^{194}\text{Pt}$, $^{18}\text{O}+^{194}\text{Pt}$, $^{18}\text{O}+^{192}\text{Os}$ and $^{19}\text{F}+^{188}\text{Os}$, by varying the value of a_f/a_n

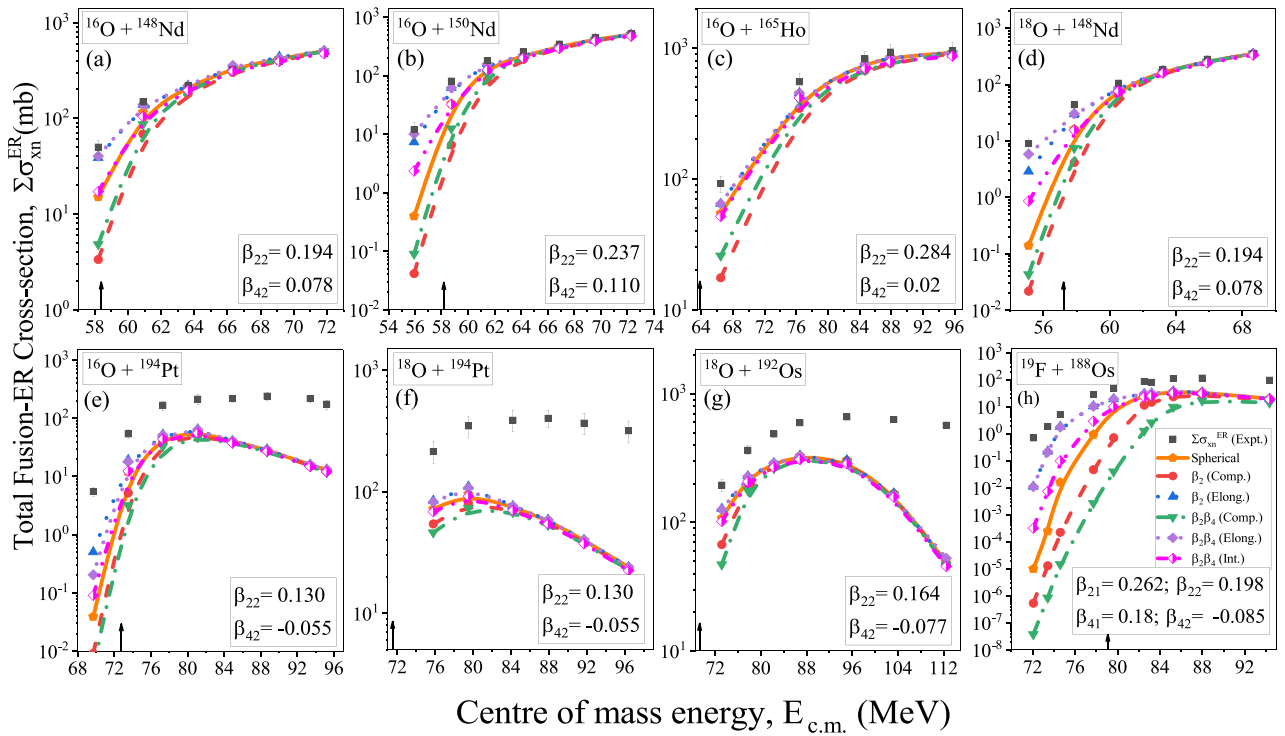


Fig. 4. (color online) Schematic diagram of total fusion-ER cross-sections ($\sum \sigma_{xn}^{\text{ER}}$) as a function of $E_{\text{c.m.}}$ with spherical, compact, and elongated configurations along with the cross-sections integrated over all the orientations of the considered P-T combinations. The black arrow denotes the Coulomb barrier energy corresponding to each P-T combination.

from 1.0 to 1.05 and compared with the cross-sections obtained with $a_f/a_n=1.1$, as shown in Fig. 6 (a-d) respectively. The figure demonstrates that the fusion-ER cross-sections vary significantly with the change in the value of a_f/a_n ratio. Based on the graph shown in Fig. 6, it can be observed that the $a_f/a_n = 1.03-1.05$ provides better agreement with the experimental data for all the considered reactions. On the other hand, the cross-sections for the reactions $^{16}\text{O} + ^{148,150}\text{Nd}$, ^{165}Ho , $^{18}\text{O} + ^{148}\text{Nd}$ persist even when the value of a_f/a_n varies from 1.0 to 1.1. This can be attributed to the higher B_f of CN. Therefore, the total fusion-ER cross-sections for all the considered reactions are collectively obtained with $a_f/a_n = 1.05$ with $\beta_2\beta_4$ deformations.

The present analysis utilized the parameters $a_f/a_n = 1.05$ and $E_d = 5.48A^{1/3}/(1+1.3A^{-1/3})$, in conjunction with the $\beta_2\beta_4$ deformation, to calculate the Fusion-ER cross-sections. Along with a_f/a_n , the damping factor (E_d) plays a crucial role in modifying the fission barrier, as shown in Eq. (23). It measures the decrease in shell correction energy that occurs with an increase in the excitation energy of the CN. In Ref. [63], the value of E_d is considered to be a constant value, that is, $E_d=25.65$ MeV. To investigate the influence of the E_d on the cross-sections, we compared the outcomes obtained from a constant E_d value of 25.65 MeV, and those obtained using the formula-based E_d expressed as $5.48A^{1/3}/(1+1.3A^{-1/3})$. The calculated ER cross-sections using both approaches facilitate a similar analysis for all the reactions under consideration, as illustrated in Fig. 7. This demonstrates that the formula-based evaluation of E_d used here aligns well with the fixed value employed in the previous studies, ensuring result consistency. Therefore, the predicted total ER cross-sections associated with $\beta_2\beta_4$ along with the ob-

served neutron channels are presented for all reactions at $a_f/a_n = 1.05$ and the formula based E_d , as illustrated in Fig. 8.

To validate the results further, we compared the cross-sections obtained from the elongated configuration and cross-sections integrated over all orientations of the $\beta_2\beta_4$ deformed nuclei, as shown in Fig. 9. This analysis revealed that, in most cases, the cross-sections from both the elongated configuration and the integrated approach yield comparable outcomes.

In addition to the O -induced reactions, we also examined $^{30}\text{Si}+^{170}\text{Er}$ to assess the aforementioned results. For this reaction, the total evaporation residue (ER) cross-sections are calculated by considering the β_2 and $\beta_2\beta_4$ deformations of both the projectile and target nuclei in their respective compact and elongated configurations. The cross-sections are also calculated by integrating across all orientations (θ_i), assuming that $a_f/a_n = 1.05$. The calculated results were subsequently compared with experimental data [64] for ER cross-sections, as illustrated in Fig. 10. Similar to previous findings, the $\beta_2\beta_4$ deformed nuclei provide better agreement with the experimental data. The results highlight the significant influence of β_2 and β_4 deformations, their corresponding orientations, and the a_f/a_n parameter in determining the fusion-ER cross-sections in this study.

IV. SUMMARY

The analysis focuses on studying the influence of deformations and associated orientations on Fusion-ER cross-sections in $^{16}\text{O} + ^{148,150}\text{Nd}$, ^{165}Ho , ^{194}Pt , $^{18}\text{O} + ^{148}\text{Nd}$, ^{194}Pt , ^{192}Os , $^{19}\text{F} + ^{188}\text{Os}$, and $^{30}\text{Si}+^{170}\text{Er}$ reactions consisting of quadrupole (β_2) and hexadecapole (β_4) deformed

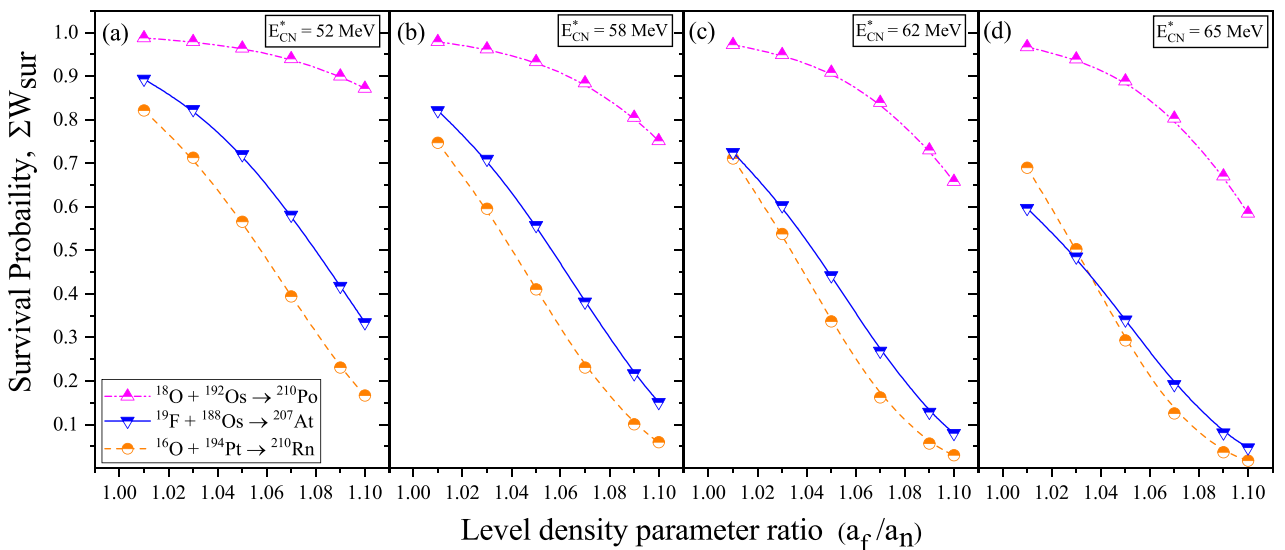


Fig. 5. (color online) Schematic diagram of the survival probability (ΣW_{sur}) for all the contributing neutron channels corresponding to CN as a function of the level density parameter ratio of the fission to neutron channel (a_f/a_n) at different magnitudes of E_{CN}^* .

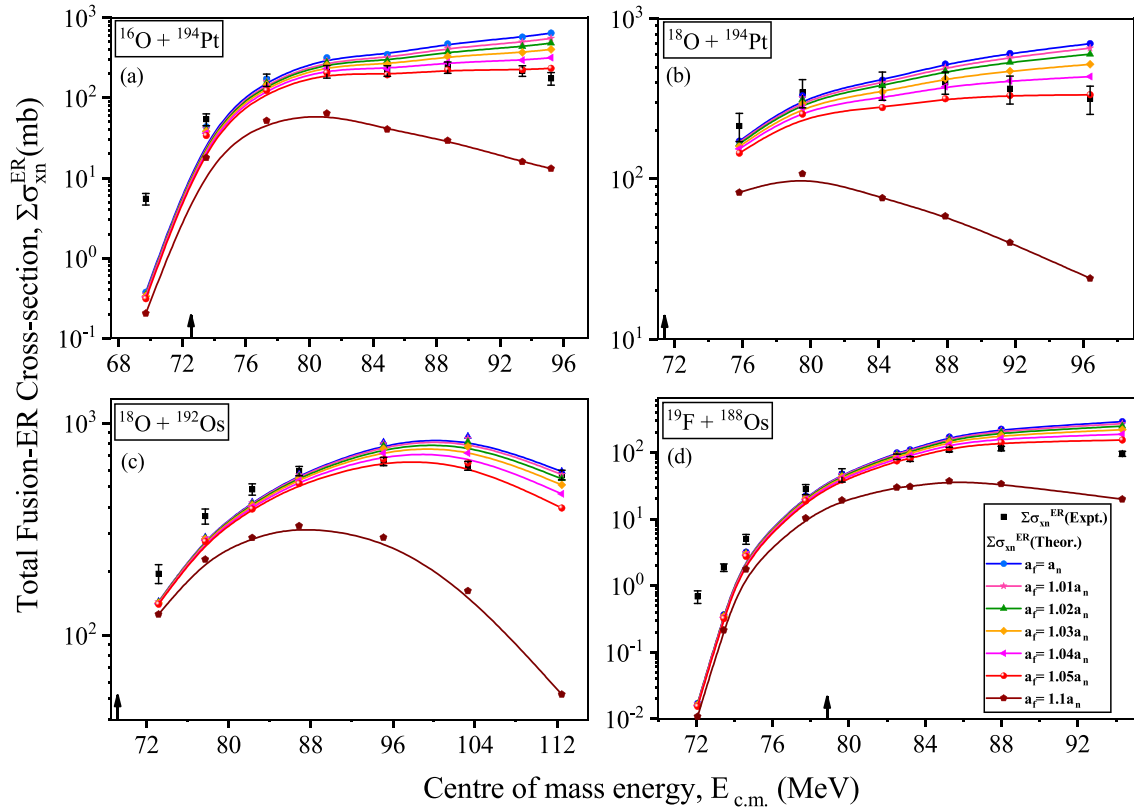


Fig. 6. (color online) Schematic diagram of the total fusion-ER cross-sections ($\Sigma\sigma_{xn}^{ER}$) as functions of $E_{c.m.}$ with the a_f/a_n ratio varying from 1.0 to 1.05 and compared with 1.1 for the reactions (a) $^{16}\text{O} + ^{194}\text{Pt}$, (b) $^{18}\text{O} + ^{194}\text{Pt}$, (c) $^{18}\text{O} + ^{192}\text{Os}$, and (d) $^{19}\text{F} + ^{188}\text{Os}$ under the influence of $\beta_2\beta_4$ with elongated configuration. The black arrow denotes the Coulomb barrier energy corresponding to each P-T combinations.

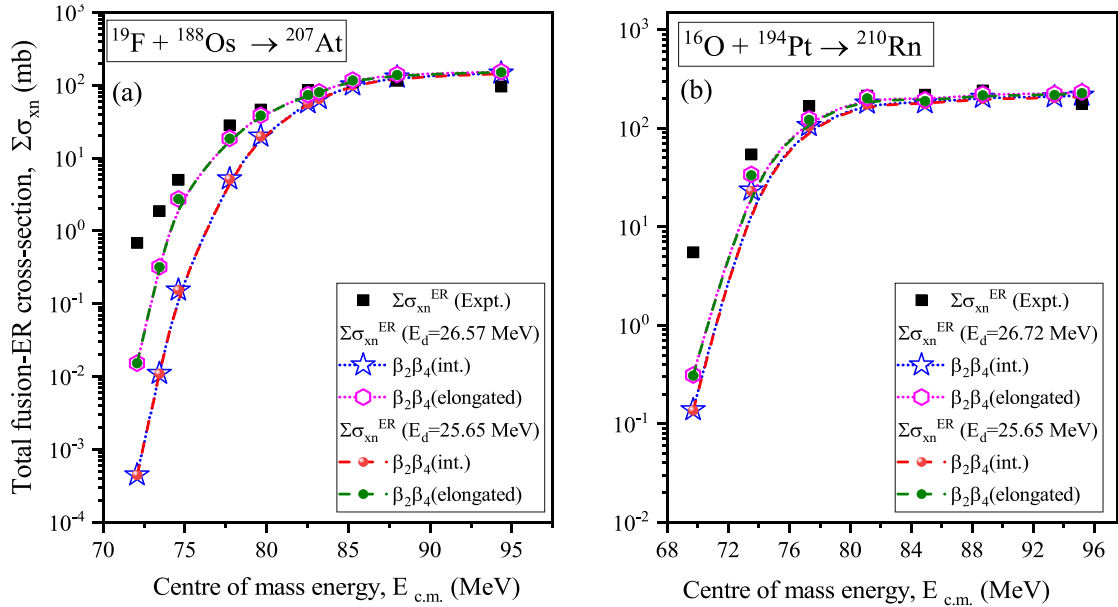


Fig. 7. (color online) Schematic diagram of total fusion-ER cross-sections ($\Sigma\sigma_{xn}^{ER}$) as a function of $E_{c.m.}$ by considering the ratio $a_f/a_n=1.05$ for P-T combinations under the influence of average orientations and the elongated configuration of $\beta_2\beta_4$ deformed nuclei with different values of E_d .

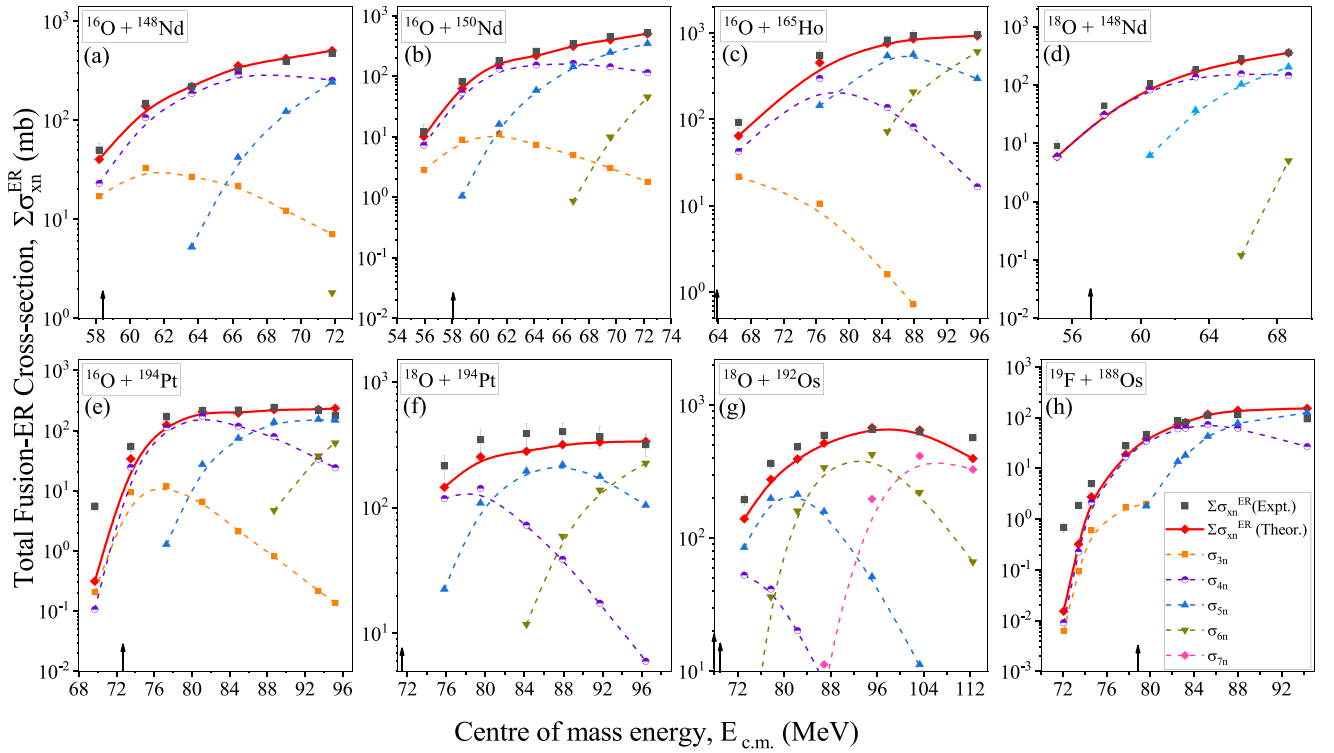


Fig. 8. (color online) Schematic diagram of the total fusion-ER cross-sections ($\sum \sigma_{xn}^{ER}$) with x-neutrons emission channels as a function of $E_{c.m.}$ at $a_f/a_n=1.05$ for all the chosen P-T combinations under the influence of $\beta_2\beta_4$ with elongated configuration. The black arrow denotes the Coulomb barrier energy corresponding to each P-T combination.

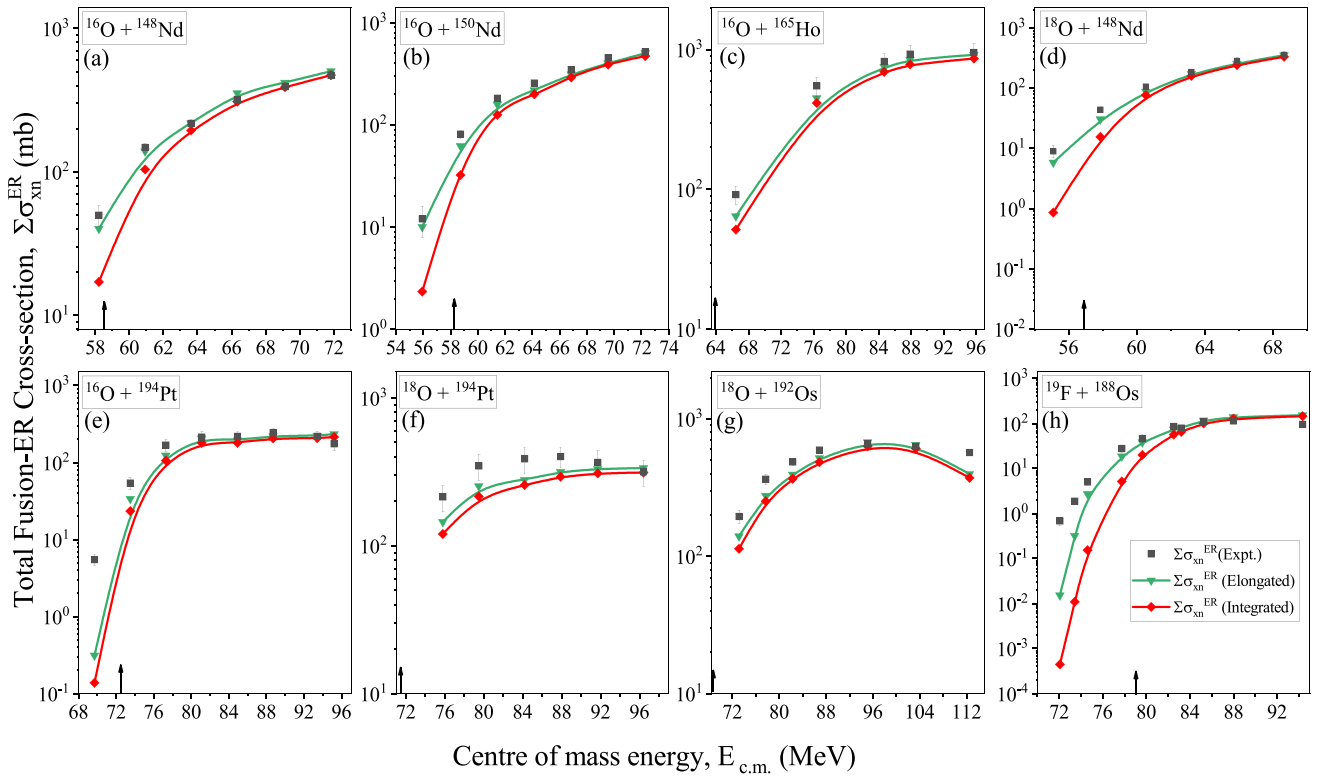


Fig. 9. (color online) Schematic diagram of the total fusion-ER cross-sections ($\sum \sigma_{xn}^{ER}$) as a function of $E_{c.m.}$ with the ratio $a_f/a_n=1.05$ for P-T combinations under the influence of average orientations and the elongated configuration of $\beta_2\beta_4$ deformed nuclei. The black arrow denotes the Coulomb barrier energy corresponding to each P-T combination.

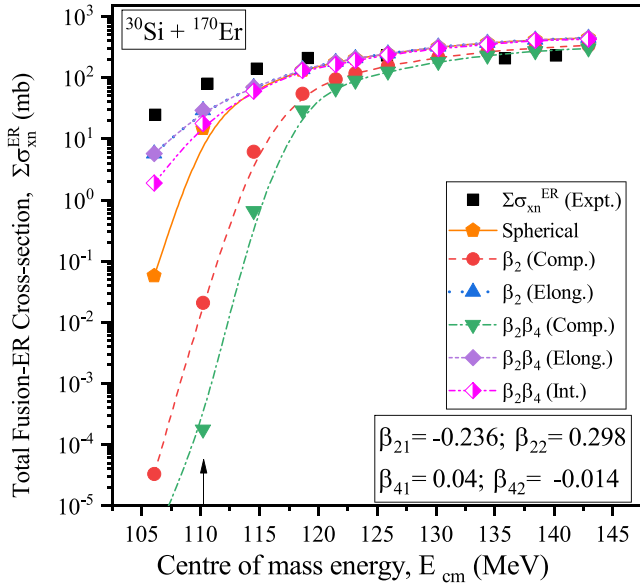


Fig. 10. (color online) Schematic diagram of the total fusion-ER cross-sections ($\sum \sigma_{xn}^{ER}$) of the $^{30}\text{Si}+^{170}\text{Er}$ reaction calculated by incorporating β_2 , $\beta_2\beta_4$ and the integrated effect of all the orientations of $\beta_2\beta_4$ deformations at $a_f/a_n = 1.05$ as function of $E_{c.m.}$. The black arrow denotes the Coulomb barrier energy corresponding to P-T combinations.

target nuclei. The influence of these parameters has been studied in terms of capture cross-section (σ_{cap}), CN formation probability (P_{CN}), survival probability (W_{sur}), and corresponding fusion-ER cross-sections for the center of mass energies ($E_{c.m.}$) lying across the barrier. The capture cross-sections (σ_{cap}) are studied within the ℓ -summed Wong model. The β_2 and β_4 deformations within the compact configuration produced hindered cross-sections compared to the spherical, whereas enhanced cross-sections are obtained at the elongated configuration. The extent of the contribution of the fusion component in the capture cross-section is studied using the compound nucleus formation probability (P_{CN}). Increasing $E_{c.m.}$ increases P_{CN} , enhancing the fusion cross-sections. In addition, the survival probability (W_{sur}) of the compound nucleus is calculated to segregate the contribution of ER and fission components. The observed discrepancy in fusion-ER reactions is attributed to the influence of the fission barrier and neutron separation energy. The survival probability of CN and subsequent ER process are addressed by adopting the appropriate level density ratio (a_f/a_n). The a_f/a_n ratio plays a dominant role in reactions with a lower fission barrier. The fusion-ER cross-sections are calculated by including $\beta_2\beta_4$ deformations at $a_f/a_n = 1.05$ and have a good agreement with experimental data.

References

- [1] W. Reisdorf and M. Schädel, *Z. Physik A - Hadrons and Nuclei* **343**, 47 (1992)
- [2] A. Karpov, V. Rachkov, and V. Saiko, *Phys. Part. Nucl. Lett.* **15**, 247 (2018)
- [3] V. Zagrebaev and W. Greiner, *Phys. Rev. C* **78**, 034610 (2008)
- [4] S. Hofmann and G. Münzenberg, *Rev. Mod. Phys.* **72**, 733 (2000)
- [5] R. N. Sagaidak, G. N. Kniajeva, Itkis *et al.*, *Phys. Rev. C* **68**, 014603 (2003)
- [6] M. Benjelloun, W. Galster, and J. Vervier, *Nucl. Phys. A* **560**, 715 (1993)
- [7] X. J. Lv, Z. Y. Yue, W. J. Zhao *et al.*, *Phys. Rev. C* **103**, 064616 (2021)
- [8] H. G. Clerc, J. Keller, C. C. Sahn *et al.*, *Nucl. Phys. A* **419**, 571 (1984)
- [9] J. X. Li and H. F. Zhang, *Phys. Rev. C* **106**, 034613 (2022)
- [10] G. G. Adamian, N. V. Antonenko, and W. Scheid, *Phys. Rev. C* **69**, 044601 (2004)
- [11] Z. H. Liu and J. D. Bao, *Phys. Rev. C* **83**, 044613 (2011)
- [12] S. Bjørnholm and W. Swiatecki, *Nucl. Phys. A* **391**, 471 (1982)
- [13] P. Fröbrich and I. Gontchar, *Phys. Rep.* **292**, 131 (1998)
- [14] D. Naderi and S. Alavi, *Phys. At. Nucl.* **81**, 196 (2018)
- [15] Y. Aritomo, T. Wada, M. Ohta *et al.*, *Phys. Rev. C* **59**, 796 (1999)
- [16] P. Sharma, B. R. Behera, *Phys. Rev. C* **96**, 034613 (2017)
- [17] R. Yanez, W. Loveland, J. S. Barrett *et al.*, *Phys. Rev. C* **88**, 014606 (2013)
- [18] P. Laveen, E. Prasad, N. Madhavan *et al.*, *J. Phys. G: Nucl. Part. Phys.* **42**, 095105 (2015)
- [19] D. Hinde, A. Berriman, R. Butt *et al.*, *Eur. Phys. J. A* **13**, 149 (2002)
- [20] R. K. Gupta, M. Balasubramaniam, R. Kumar *et al.*, *J. Phys. G: Nucl. Part. Phys.* **31**, 631 (2005)
- [21] H. Sharma, S. Jain, R. Kumar *et al.*, *Phys. Rev. C* **108**, 044613 (2023)
- [22] L. Zhu, Z.-Q. Feng, C. Li *et al.*, *Phys. Rev. C* **90**, 014612 (2014)
- [23] R. G. Stokstad, Y. Eisen, S. Kaplanis *et al.*, *Phys. Rev. Lett.* **41**, 465 (1978)
- [24] N. Wang, E. G. Zhao, W. Scheid *et al.*, *Phys. Rev. C* **85**, 041601 (2012)
- [25] M. Shareef, E. Prasad, A. Jhingan *et al.*, *Phys. Rev. C* **99**, 024618 (2019)
- [26] R. Lemmon, J. Leigh, J. Wei, *et al.*, *Phys. Lett. B* **316**, 32 (1993)
- [27] M. Ismail, W. Seif, and M. Botros, *Nucl. Phys. A* **828**, 333 (2009)
- [28] T. Rajbongshi, K. Kalita, S. Nath *et al.*, *Phys. Rev. C* **93**, 054622 (2016)
- [29] N. Jain, M. Bhuyan, and R. Kumar, *Phys. Scr.* **98**, 025303 (2023)
- [30] K. S. Choi, K. S. Kim, M. K. Cheoun *et al.*, *Phys. Rev. C* **103**, 034611 (2021)
- [31] C. Simenel, M. Dasgupta, D. J. Hinde *et al.*, *Phys. Rev. C* **88**, 064604 (2013)
- [32] T. Izumoto, T. Udagawa, and B. T. Kim, *Phys. Rev. C* **51**, 761 (1995)
- [33] A. Adel and T. Alharbi, *Eur. Phys. J. A* **53**, 1 (2017)

- [34] Vijay, R. P. Chahal, M. S. Gautam *et al.*, *Phys. Rev. C* **103**, 024607 (2021)
- [35] R. Broda, M. Ishihara, B. Herskind *et al.*, *Nucl. Phys. A* **248**, 356 (1975)
- [36] K. Kumar, T. Ahmad, S. Ali *et al.*, *Phys. Rev. C* **87**, 044608 (2013)
- [37] R. Charity, J. Leigh, J. Bokhorst *et al.*, *Nucl. Phys. A* **457**, 441 (1986)
- [38] K. Mahata, S. Kailas, A. Shrivastava *et al.*, *Nucl. Phys. A* **720**, 209 (2003)
- [39] E. Prasad, K. M. Varier, N. Madhavan *et al.*, *Phys. Rev. C* **84**, 064606 (2011)
- [40] J. Błocki, J. Randrup, W. Świątecki *et al.*, *Ann. Phys.* **105**, 427 (1977)
- [41] K. Siwek-Wilczyńska, A. Borowiec, I. Skwira-Chalot *et al.*, *Int. J. Mod. Phys. E* **17**, 12 (2008)
- [42] E. Cherepanov, A. Iljinov, and M. Mebel, *J. Phys. G: Nucl. Phys.* **9**, 931 (1983)
- [43] C. Wong, *Phys. Rev. Lett.* **31**, 766 (1973)
- [44] R. Kumar, M. Bansal, S. K. Arun *et al.*, *Phys. Rev. C* **80**, 034618 (2009)
- [45] W. Scobel, H. H. Gutbrod, M. Blann *et al.*, *Phys. Rev. C* **14**, 1808 (1976)
- [46] D. L. Hill and J. A. Wheeler, *Phys. Rev.* **89**, 1102 (1953)
- [47] A. Bohr, *Dan. Mat. Fys. Medd.* **26**, 1 (1952)
- [48] A. N. Bohr and B. R. Mottelson, *Dan. Mat. Fys. Medd.* **27**, 1 (1953)
- [49] P. Möller, A. J. Sierk, T. Ichikawa *et al.*, *At. Data Nucl. Data Tables* **109**, 1 (2016)
- [50] R. Smolańczuk, *Phys. Rev. C* **56**, 812 (1997)
- [51] R. K. Gupta, N. Singh, and M. Manhas, *Phys. Rev. C* **70**, 034608 (2004)
- [52] D. A. Mayorov, T. A. Werke, M. C. Alfonso *et al.*, *Phys. Rev. C* **90**, 024602 (2014)
- [53] T. A. Werke, D. A. Mayorov, M. C. Alfonso *et al.*, *Phys. Rev. C* **92**, 034613 (2015)
- [54] . Santhosh and V. Safoora, in *Nuclear Structure Physics* (CRC Press, 2020) pp. 185–202.
- [55] J. Jackson, *Can. J. Phys.* **34**, 767 (1956)
- [56] K. Le Couteur and D. Lang, *Nucl. Phys.* **13**, 32 (1959)
- [57] A. Rahmatinejad, T. Shneidman, G. Adamian *et al.*, *Phys. Lett. B* **844**, 138099 (2023)
- [58] R. Vandenbosch and J. Huizenga, *Nuclear Fission* (New York: Academic Press, 1973)
- [59] M. Dahlinger, D. Vermeulen, and K.-H. Schmidt, *Nucl. Phys. A* **376**, 94 (1982)
- [60] V. Singh, B. R. Behera, M. Kaur *et al.*, *Phys. Rev. C* **89**, 024609 (2014)
- [61] A. Rahmatinejad, T. M. Shneidman, G. G. Adamian *et al.*, *Phys. Rev. C* **105**, 044328 (2022)
- [62] B. Wang, Z. Y. Yue, and W. J. Zhao, *Phys. Rev. C* **103**, 034605 (2021)
- [63] Y. Fang, Z. Gao, Y. Zhang *et al.*, *Phys. Lett. B* **858**, 139069 (2024)
- [64] D. Hinde, J. Leigh, J. Newton *et al.*, *Nucl. Phys. A* **385**, 109 (1982)